Progression of Reduction of MoO_3 Observed in Powders and Solution-Processed Films

*Katherine Inzani[a], Mohammadreza Nematollahi[b], Sverre M. Selbach[a], Tor Grande[a] and Fride Vullum-Bruer[a]**

[a]Department of Materials Science and Engineering, Norwegian University of Science and Technology, N-7491 Trondheim, Norway

[b]Department of Physics, Norwegian University of Science and Technology, N-7491 Trondheim, Norway

Corresponding Author

*Phone: +47-73-59-39-76; e-mail: fride.vullum-bruer@ntnu.no

Abstract

Understanding the reduction of MoO_3 is important for the utilization of this material in optoelectronic applications. Here, we examine the changes that take place during reduction of a solution-processed thin film of MoO_3. Upon reduction in dilute hydrogen gas, the nanocrystallite grain morphology is observed hosting a sequence of shear defects, nucleation and growth of reduced molybdenum oxide phases within the MoO_3 matrix before decomposition of the film. The compositional changes are tracked and compared with changing optical properties. The formation of extended defects is associated with enhanced photoluminescence. The progression of reduction in the films is highly related to reduction of powders and should be considered when designing devices utilizing MoO_{3-x}.

Keywords

Reduced molybdenum oxides; Phase evolution; Solution processing; Film morphology; Shear planes; Rapid thermal processing; Photoluminescence.

1 Introduction

Molybdenum trioxide, MoO_3, is a wide band gap semiconductor with applications in optoelectronics such as organic light emitting diodes (OLEDs), photovoltaics and photodetectors, as a multichromic material in smart windows and displays, as a catalyst and in emerging energy storage technologies [1–9]. Common to all these applications is the importance of its electronic structure, which is heavily dependent on the oxygen stoichiometry [10,11]. MoO_3 is often utilized in an oxygen deficient form, either being reduced in use as a catalyst, or being used as MoO_{3-x} in optoelectronic devices with oxygen vacancies vital to operation [12–15]. Alternatively, certain applications of MoO_3 require strict oxygen stoichiometry with oxygen vacancies being detrimental to performance, for example in OLEDs [5,16,17]. The range of stoichiometries at which MoO_{3-x} is utilized spans from x = 0 to x = 1 [12,14]. This range includes extended defect states such as shear structures and other phases such as Mo_4O_{11} and MoO_2 which may be present alongside MoO_3. There is a complex sequence of reduction which has mainly been studied in single crystals and powders [10,18–22]. Decades of research have uncovered seemingly incompatible observations and the exact reactions taking place remain controversial. This is partly because the reaction kinetics are extremely dependent on experimental conditions [21,23–28]. However, MoO_{3-x} is often utilized as a thin film, especially in electronic devices, and such films will have even greater sensitivity to kinetics due to high surface areas and associated strains [29–33]. The mechanisms of reduction in thin films may therefore vary greatly from powders to films, and a better knowledge of film reduction is required for optimal device fabrication.

The thermodynamically stable polymorph of molybdenum oxide is α-MoO_3, a layered structure with space group *Pbnm*, shown in Figure 1. The structure is characterized by layers of octahedra bound by dispersed forces, with interlayer spaces known as the van der Waals gap. There are oxygen ions on three inequivalent sites at octahedral apices (O1), corner-

sharing (O2) and edge-sharing (O3) positions. Oxygen is readily removed from the structure and it is thought that the apical O1 oxygen is the most easily removed. This is intuitive based on its orientation towards the van der Waals gap and is supported by computation of defect formation energies [34].

The range of x for which vacancies are present as isolated point defects is very small, only up to x = 0.001 [18]. Beyond this, a complex sequence of extended defect structures occurs, which have been studied extensively by transmission electron microscopy of single crystals [10,18,20,35–37]. The defect structures progress through several phases based on shear of the MoO_3 lattice, such as $Mo_{18}O_{52}$ [35]. Movement of the crystallographic shear planes has been linked to the formation of MoO_2 nuclei. In powders, there has been much contention in the reactions occurring in the reduction of MoO_3 to MoO_2. There has been one proposed mechanism that accounts for all the observed phenomena reported, in which the autocatalytic topotactic transformation $MoO_3 \rightarrow MoO_2$ takes place simultaneous to the comproportionation of $MoO_3 + MoO_2 \rightarrow Mo_4O_{11}$ [21]. A mixture of these phases, plus shear structures based on both MoO_3 and MoO_2 type lattices, can be present during the reduction. On the reduction of films, many studies have found synthesis variables for specific device properties which are often an effect of stoichiometry changes. Variables affecting stoichiometry in the production of MoO_{3-x} films include the ambient and substrate conditions in physical depositions and decomposition of precursors in solution processing [6,7,29,30,38–43]. Post-annealing has been the subject of several studies [6,7,30,40–42]. These have associated changes in optical and electrical properties with vacancy concentration, after treatment in oxidizing or reducing environments, or under ultraviolet light.

The possible configurations of Mo ions in various oxides are appealing for emerging technologies where tuning of electronic structure is needed. For example, MoO_{3-x} has been proposed as an intermediate band photovoltaic material, for which a precise control of gap

states is required [44,45]. For this, as well as for optimisation in current applications, insight into the mechanism of film reduction is required. To this end, changes in morphology, crystallinity, chemical state and optical properties are explored during reduction of solution-processed MoO_3 films in hydrogen atmosphere. The progression of reduction is compared to that observed in powders.

2 Experimental Details

2.1 Synthesis route and reduction

Ammonium heptamolybdate tetrahydrate ($(NH_4)_6Mo_7O_{24}\cdot 4H_2O$, referred to as AHM, 99.98% trace metals basis, Sigma-Aldrich) was used as a precursor. To obtain crystalline MoO_3 powders, AHM was ground in a mortar and heated to 500 °C in air at a heating rate of 100 °C/h and held for 3 h. The MoO_3 powder was ball milled for 24 h with 5 mm YSZ balls in ethanol absolute and then dried at 80 °C. Powders were reduced in 5 % H_2/95 % Ar for up to 18 h at temperatures from 400 °C to 500 °C.

All solution and film preparation was done in an ISO7 cleanroom (NTNU NanoLab). Solutions for spin coating films were made by dissolving AHM in deionized water to make a 0.5 mol[Mo]L^{-1} solution and adjusting the pH to 8-10 with 25 % ammonia solution (Merck Millipore) to prevent MoO_3 precipitating. Solutions were stirred on a hotplate at 50 °C for 30 min and then sonicated for 10 s to degas. Quartz substrates (Spectrosil® synthetic fused silica, 1 mm thickness, UQG Optics) were prepared by cleaning in ethanol followed by oxygen plasma cleaning for 5 min to activate the surface (Diener Electronic, FEMTO Plasma Cleaner). Solutions were applied to the substrates through a syringe with a 0.2 μm filter (Acrodisc, Pall) and spin coated at 2500 rpm for 1 minute (Laurell WS-400B-6NPP-Lite Spinner). Heat treatment of the films was done in a rapid thermal process furnace (RTP, Jipelec JetFirst 200 Processor) at a heating rate of 6 K/s to 200-500 °C, holding for 10

minutes in an oxygen atmosphere flowing at 200 sccm. For precise control of the reduction degree, a rapid thermal process was also used for reduction of the films. This was done in 5 % H_2/95 % Ar flowing at 1000 sccm, held at various temperatures for 30 minutes.

2.2 Labels of the samples

Sample names of powders are composed of a P and the temperature for reduction in 5 % hydrogen, held for 18 hours (P-0 is not reduced; P-400 and P-500). Labels of the films include an F and the temperature at which the films were reduced in the RTP process in 5 % H_2 for 30 minutes (F-0 is not reduced; F-200, F-300, F-350, F-400, F-450 and F-500).

2.3 Characterization

Thermogravimetric analysis (TGA, Netzsch, STA 449 C) of AHM in transformation to MoO_3 was performed by heating powders up to 600 °C in synthetic air with a flow rate of 30 sccm and a heating rate of 10 K/min. For TGA of MoO_3 powders during reduction, the samples were initially heated to 400 °C for 10 minutes to remove adsorbed water and CO_2, followed by heating from room temperature to 400 °C and 500 °C at a heating rate of 10 K/min and holding at each temperature for 18 h in 2 % H_2/98 % Ar flowing at 30 sccm. The lower H_2 percentage was used to protect the apparatus, and provides a less reducing atmosphere than the higher H_2 percentage used for the powder and film samples. X-ray diffraction (XRD) was done to determine the phase composition of the powders and films. A Bruker D8 Advance DaVinci X-ray Diffractometer with LynxEye™ SuperSpeed Detector was used for powder analysis and a Bruker AXS D8 Focus with Solid state LynxEye™ detector was used for film analysis. CuKα radiation source was used in Bragg-Bretano geometry (0.01° step size, 1.5 s step time and 10° to 60° 2θ). Scanning electron microscopy (FEG-SEM, Zeiss Ultra 55 Limited Edition) was performed to determine the morphology of the powders and films, for which films were coated with a thin layer of carbon to prevent charging. Film surfaces were

investigated at by atomic force microscopy (AFM, Veeco Multimode V, Nanoscope software) with Peak Force Tapping™ in ScanAsyst mode. Film thickness was measured by profilometry (Veeco Dektak 150), after etching a step to the substrate with 0.05 M NaOH solution. Samples F-450 and F-500 had too high a roughness to have thickness measured by this method.

X-ray photoelectron spectroscopy (XPS) was used to analyze the change in chemical composition of the powders and films after reduction. XPS was obtained with a Kratos Axis Ultra spectrometer using a monochromatic Al Kα X-ray source (hv = 1486.6 eV, 15 mA, 15 kV, pass energy 20 eV, energy resolution 150 meV). The analysis area was 300 µm - 700 µm for all samples, and the spectra were collected with a photoelectron take-off angle of 90 degrees. Samples were isolated from the stage to avoid partial charging, and the Kratos charge neutralizer system was used. The binding energies (Eb) were corrected by Eb equal to 284.8 eV of adventitious C1s. Background modeling and subtraction, peak fitting and quantification of the components were processed using CasaXPS software (version 2.3.16). Prior to peak fitting, an offset Shirley background was subtracted from the spectrum. The offset Shirley background was calculated from a blend of a Shirley and linear backgrounds $OS(E:\lambda) = S(E)(1-\lambda) + L(E)\lambda$ where the Shirley and the linear background are represented by $\lambda = 0$, and $\lambda = 1$, respectively. In the curve fitting models, $\lambda = 0.3$ was used for all the components. For Mo 3*d* and Mo 3*p* peaks a LF(α, β, w, m) line shape was used, which is a Lorentzian line shape available in CasaXPS which includes consideration of the Gaussian instrumental broadening. All Mo 3*p* peaks were symmetrical, whilst Mo 3*d* peaks had a slightly asymmetric line shape. Relative content of Mo oxidation states were derived from the ratio of peak areas of the deconvoluted Mo 3*d* curves.

A UV/Vis/NIR spectrophotometer (OLIS 14) was used to measure the transmittance of the films over the range 250 – 2100 nm. Low-temperature (10 K) photoluminescence

measurements were performed on the films using a high-sensitivity imaging spectrometer, JobinYvonHoriba iHR320, coupled with an electron multiplying charge-coupled device in imaging geometry. Excitation source was the 325 nm line of a cw He-Cd laser at 6 mW. The spectra were corrected for system sensitivity changes with wavelength by multiplying to the response function of the system. The raw data is presented alongside the corrected data.

3 Results and Discussion

3.1 Powders

Thermogravimetrical analysis of the two synthesis steps, decomposing AHM to MoO_3, and reducing MoO_3 to MoO_{3-x}, are presented in Figure 2. In the thermal decomposition of AHM powder in air, Figure 2a, the mass loss onset at 100 °C corresponds to loss of water from the complex, and the two steps at 93 % and 89 % of the starting mass are likely compounds of the form $(NH_4)_2O{\cdot}xMoO_3$ [46]. The temperature ranges of these processes are 100 – 140 °C and 195 – 240 °C, respectively. The third transformation begins at 290 °C and the end composition is reached at 400 °C, at 81.7 % of the starting mass. This is confirmed to be α-MoO_3 by XRD (P-0 in Figure 3). Isothermal annealing in 2 % H_2/98 % Ar at 400 °C, 450 °C and 500 °C results in approximately linear mass loss (Figure 2b). The rate of mass loss is highly dependent on the annealing temperature. For calculating stoichiometry, we can assume a starting composition of $MoO_{2.98}$ based on XPS analysis of the starting powder (Table 1). However, this is likely an overestimate of oxygen deficiency due to surface reduction of the powder and the surface sensitivity of XPS measurement. Attributing mass losses to oxygen only, at 400 °C the mass loss corresponds to a stoichiometry of $MoO_{2.96}$ after 18 h, compared to $MoO_{2.90}$ at 450 °C and $MoO_{2.72}$ at 500 °C. These end compositions are not equivalent to

the following powder samples because of the less reducing atmosphere used in the thermogravimetric measurement.

Sample P-0 is orthorhombic MoO_3, as shown in the X-ray powder diffractograms in Figure 3a. For P-400, after holding for 18 h at 400 °C in 5 % H_2/95 % Ar, MoO_3 remains as the main phase and MoO_2 reflections appear. MoO_2 is confirmed to be the first detectable secondary phase to form with a series of reductions at 400 °C held for shorter times (Figure 3b). For P-500, after a 500 °C treatment for 18 hours there are no MoO_3 reflections remaining, while both MoO_2 and Mo_4O_{11} are present in the powder.

There is a change in the powder morphology with annealing, displayed in the SEM images in Figure 4. The P-0 powders are platelets ranging from 100 - 700 nm in diameter, with 100 - 150 nm thickness. Facets are present on the surface of the platelets. In sample P-400 there are large agglomerates, over 1 µm wide, that appear to be made up of the smaller platelets. In the P-500 sample there are two distinct types of particles present; large crystallites from 2 to 4 µm wide with well-defined facets, and smaller particles less than 500 nm diameter and irregularly shaped.

The observations here show MoO_2 to nucleate on MoO_3 first, at 400 °C, at the same stage of reduction as agglomeration of MoO_3 platelets takes place. Following this, at 500 °C, the mixture of MoO_2 and Mo_4O_{11} phases identified by XRD is reflected by the two distinct particle morphologies. The morphology of the large crystals indicates them to be Mo_4O_{11}, in comparison with powders observed by Schulmeyer *et al.* [22] Based on the similarity in sizes, the transformation to large crystallites likely occurs from the agglomerates.

XPS spectra for the powder samples are shown in Figure 5 and analysis of Mo oxidation state from Mo 3*d* peaks is given in Table 1. Deconvolution of the Mo 3*d* spectra for sample P-0 revealed that molybdenum is mainly Mo^{6+} (94.7 %) with a small amount of Mo^{5+} (5.3 %). A

similar amount of Mo^{5+} remained even after annealing in air at 400 °C, and as the samples were exposed to atmosphere before XPS analysis this Mo^{5+} can be attributed to surface reduction [47]. This is also seen in the filling of the Mo 4*d* states in the valence band region, from 0.4 to 2.1 eV.

Sample P-400 demonstrates an increased amount of Mo^{5+} compared to P-0 (12.9 %), in addition to the presence of 2.1 % Mo^{4+}. The true content of Mo^{4+} is likely to be higher than this due to atmospheric oxidation of the surface. This is in keeping with the XRD results that P-400 is mainly MoO_3 with a small amount of MoO_2. As no other crystalline phases were detected by XRD, the Mo^{5+} content can be attributed to oxygen vacancies in the MoO_3 lattice. The P-500 sample contains a much higher amount of Mo^{4+} (48.7 %), which reveals that almost half of the sample is converted to MoO_2. The remainder is Mo^{6+} and Mo^{5+} in close to equal proportions, which corresponds to the distribution of oxidation states in Mo_4O_{11}. This is in agreement with the XRD analysis and the two-phase mixture of particles seen in SEM. There is also a high intensity in the binding energy between Mo^{5+} and Mo^{4+}. This is accounted for by considering four peaks related to the Mo^{4+} oxidation state, that is the screened and unscreened peaks in the model of Scanlon *et al.* [48]. To calculate the Mo^{4+} content, the total area of the screened and unscreened peaks have been used.

In addition, from deconvolution of the O 1*s* high resolution spectra, of which the main peak is attributed to the oxygen bonded to molybdenum, a shift to lower binding energy is observed for P-500 compared to P-0 and P-400 (Figure 5c). This can be attributed to the large amount of MoO_2 present. The structure of the valence band also changes with reduction. The valence band is largely made up of O 2*p* states and the conduction band of metal 4*d* states. Stoichiometric MoO_3 would have unoccupied 4*d* states as Mo^{6+} has $4d^0$ configuration, whereas oxygen deficiency populates these states, which appear as a peak at 1-2 eV [10]. Sample P-400 shows greater filling of the Mo 4*d* states compared to P-0, related to the

presence of Mo^{5+} in the form of lattice defects. Both P-0 and P-400 exhibit a structure in the O 2*p* states, due to the asymmetry of Mo–O bonding in the crystal structure of MoO_3. There are peaks at 7 and 9 eV as a result of the Mo 4*d* contribution to the valence band [11,48]. With P-500, this feature of the O 2*p* states is lost but two distinct peaks emerge in the Mo 4*d* states, which is attributed to Mo–Mo bonding in the distorted rutile structure of MoO_2 [48].

The sequence of reduction in the powders is concurrent with the mechanism proposed by Lalik *et al.* in which MoO_2 nucleates by a topotactic mechanism from the removal of oxygen from MoO_3, followed by further reduction of MoO_3 to MoO_2 alongside re-oxidation of MoO_2 to Mo_4O_{11} in a comproportionation reaction, utilizing the oxygen released from the MoO_3 lattice [21]. The P-500 sample corresponds to a point after the MoO_3 has been consumed, when there is no oxygen available for further oxidation, and the Mo_4O_{11} phase is being reduced to MoO_2. It is also noted that the temperature during reduction of MoO_3 can affect the mechanism of reduction, and a consecutive reaction mechanism is also a possible explanation for these results [49].

3.2 Films

After deposition, the AHM films required annealing in air at 400 °C for 10 minutes to appear crystalline by XRD. XRD diffractograms of the non-reduced and reduced samples are shown in Figure 6. In all scans there is an amorphous background present from the quartz substrate. Reflections due to MoO_3 are seen for samples F-0, F-200, F-300, F-350, F-400 and F-450. The highest intensity reflections are indexed to the (020), (040) and (060) *hkl* planes, indicating film or crystallite orientation along the {020} planes. The intensity of the reflections is reduced in F-400 and drastically reduced in F-450. This demonstrates a decrease in the amount of MoO_3 phase present in the films. Sample F-450 has additional faint reflections at the positions of the main diffraction lines of Mo_4O_{11}, indicating the onset of

formation of this phase at 450 °C. In F-500, however, only faint MoO_3 reflections remain and a broad reflection appears at 41°, which matches to Mo metal.

The XPS spectra of the Mo 3*d* and 3*p* peaks of the reduced films with deconvolution to different oxidation states are displayed in Figure 7. Table 2 shows the analysis of the oxidation states by deconvolution of Mo 3*d* and 3*p* peaks. Mo 3*d* is reliable for all films except F-500 for which Mo 3*p* is referred to. Films F-200 and F-300 are mainly Mo^{6+} with a similar Mo^{5+} content to each other and no Mo^{4+} present. The proportion of Mo^{5+} is similar to the surface reduction of the unreduced powder sample, P-0. In addition, the valence band region shows only low levels of Mo 4*d*. This suggests that up to 300 °C hydrogen treatment does not considerably increase the amount of oxygen vacancies in the films, nor does it cause MoO_2 to form. Increasing the reduction temperature to 400 °C, the film remains mainly Mo^{6+} but there is an increase in the Mo^{5+} content to 9.4%. There is also an increase in the filled Mo 4*d* states at the valence band and a loss of definition in the O 2*p* valence band features. There is no Mo^{4+} which shows that MoO_2 is absent. The Mo^{5+} content could be point defects, extended defects, amorphous phases or undetected reduced molybdenum oxide phases. Due to the similarity of the F-300 and F-400 films, XPS analysis of the F-350 film is omitted. The F-450 film is still mainly Mo^{6+} with 15.1% Mo^{5+} and 3.6% Mo^{4+}. The Mo^{6+} and Mo^{5+} are likely to be partially in Mo_4O_{11} phase, as seen in XRD. The presence of Mo^{4+} and the emergence of split Mo 4*d* peaks in the valence band region suggest that there is MoO_2 in the film. It is likely that this small amount of MoO_2 is below the detection limit of XRD. The F-500 film is mainly metallic Mo^0. The remainder consists of Mo^{4+}, Mo^{5+} and Mo^{6+}, which can be partially due to oxidation of the metallic surface, and may also exist in remaining oxide phases which are only faintly detected by XRD.

The SEM micrograph of an unreduced MoO_3 film in Figure 8 shows that the film is flat and continuous, with no particles or pinholes on the surface. This is representative of a large area

of the film. It consists of grains of a few microns in diameter, with a series of parallel lines within some of the grains.

The root mean square (RMS) roughness (Rq) is 1.53 nm, as measured by AFM over a 10 μm x 10 μm area. AFM further reveals the films to have a polycrystalline grain structure, shown in Figure 9a, with grains composed of oriented nanocrystallites. The grain can be defined as a region of oriented nanocrystallites, and the grain boundary is where the nanocrystallites of different orientations intercept. The nanocrystallites are platelet-like, greater than 100 nm in length and less than 10 nm thick. The unreduced F-0 film has two types of linear features indicated by arrows (i) and (ii). The lines at (i) are parallel to the alignment of the nanocrystallite platelets; they span the grain and are spaced a few hundred nanometres apart, and outline a stepped topography within the grain. The lines at (ii), however, are perpendicular to the nanocrystallite orientation and actually cut through the material. These could be misfit defects or cracks that may occur on cooling. The thickness of the unreduced film was measured as 60 nm ± 5nm, and there was negligible change in thickness of the reduced films (Table 3). Upon reduction, there are several changes seen in the films by AFM. Firstly, there is an increasing RMS roughness with reduction temperature, as shown in Table 3. Rq remains low, below 2 nm, up to 400°C, and then there is a factor of 10 increase for F-450. There are no other differences visible by AFM between the F-0, F-200, F-300 and F-350 films. Figure 9 shows the similarity between films F-0 and F-350 and the differences developed in F-400 and F-450. There are several developments within the F-400 film. The arrow at (iii) shows a 175 x 450 nm region of oriented growth at a triple point grain boundary, likely to be crystal nucleation. At point (iv), faint lines appear intersecting the nanocrystallite alignment at an angle of approximately 30°. In studies of oxygen vacancies in single crystals of MoO_3, it was found that vacancies were accommodated by shear on crystallographic shear planes indexed to $(\bar{1}20)$ and (120) [18]. The angle at which the shear

planes meets the (010) plane, that is, the layers within the MoO_3 crystal (Figure 1), is 26.6°. That this angle coincides with the direction of the faint lines in the films is evidence for a similar shear mechanism happening across the nanocrystallites. Furthermore, the arrows at (v) and (vi) indicate growth within the grains along lines at a similar angle. This growth is seen across the entirety of the film, consistently at this angle to the nanocrystallite direction. Thus, it is proposed that shear planes across the grain accommodate oxygen vacancies as the film is strained during reduction, and these shear planes act as nucleation sites for a reduced phase of molybdenum oxide. The shear planes may exist in an intermediate phase such as $Mo_{18}O_{52}$, which cannot be distinguished by XRD [8,26]. Upon further reduction, the F-450 film exhibits further growth of a new phase, both within the original grains structure and as developed larger crystals of the order of 1 μm. The highly faceted character of this phase has similarities with the reduced phase in the powders that was proposed to be Mo_4O_{11}. In addition, as this coincides with the appearance of Mo_4O_{11} reflections in the X-ray diffraction patterns, it is a reasonable assumption that these features are Mo_4O_{11}.

Transmission spectra of the films in the reduction series are illustrated in Figure 10a. The unreduced film F-0 has transmittance greater than 70 % in the visible region. The transmittance decreases upon reduction, up to 34 % for the film F-500. There is an absorption tail present near 280 nm for all films. The absorption edge is shifted to longer wavelengths with increasing treatment temperature. The decrease in transmittance with increased reduction temperature may not be entirely due to increased reduction degree, as there may be effects of film thickness present. Optical constants cannot be extracted due to the small film thickness. Instead, the optical band gap can be discussed as a measure of absorption independently of film thickness.

The optical band gap of the films, E_g, is estimated by a Tauc plot, utilizing the relation,

$(\alpha hv)^n = A(hv\text{-}E_g)$

where α is the absorption coefficient, *h* is the Planck constant, *v* is the frequency of light and *A* is the band edge parameter. The exponent *n* is set as 2 for allowed direct transitions, which gave a linear relation [50]. α is defined by transmittance $T = e^{-\alpha z}$ where *z* is the optical path length which is taken as the film thickness (60 nm). The Tauc plot of $(\alpha hv)^2$ versus photon energy (hv) is shown in Figure 10b. E_g of the films was evaluated by fitting the linear region of the plot to zero and are listed in Table 3. The error accounts for the choice of linear region within the curve. The band gap generally decreases with increasing reduction temperature, from 2.7 eV for F-0 to 1.0 eV for F-500. F-200, F-300 and F-350 have a similarly high E_g compared to those films reduced at higher temperatures. Decrease of E_g is due to the formation of defects or reduced phases which form states within the band gap. This is known to occur with oxygen vacancies in MoO_3 [30,40,42]. The high E_g maintained up to F-350 can be associated with structural rearrangements in the lattice which reduces the number of point defects even with increased reduction. This is further discussed in combination with the photoluminescence data below.

Figure 10 also displays the photoluminescence spectra of the films F-0 to F-400. The raw and instrument spectral response corrected data are shown in (c) and (d), respectively. For all films, there is one broad band seen in the raw data, centred at 464 nm, with several small peaks distinguishable. After spectral correction, a broad band is visible at 375-400 nm, the peak of which is at 388 nm. This band corresponds to near band emission (NBE) due to free-exciton recombination [51]. The band centred at 464 nm is attributed to deep level emission (DLE), which is related to lattice imperfections such as vacancies or extended defects [51]. The intensity of the DLE can also be contributed to by band-to-band absorption that results in emission at higher wavelengths than the NBE due to thermalization. The spectra exhibit weak peaks 445 nm, 464 nm, 475 nm and 514 nm. These represent intraband radiative

recombination, for instance from various Mo^{5+} *d-d* transitions [51–54]. The broad DLE band suggests that a continuum exists rather than discrete states in the band gap. These features are typical for MoO_3 nanostructures, as demonstrated in several studies [51,55–57]. The films differ in intensity of PL response and in the ratio of the intensity of the NBE and DLE bands. All films that have undergone a reduction treatment show stronger PL than the not-treated film. There are several factors that can contribute to increased PL, including an increase in radiative recombination centres, decrease in non-radiative recombination centres, and increase in surface roughness or porosity. As all reduced films have a higher surface roughness than the non-reduced film F-0, as measured by AFM, this will result in stronger absorption and a corresponding stronger PL response. The change in the intensity ratio NBE/DLE can rather be due to a change in the number of radiative and non-radiative recombination centres. It is interesting that there are differences between the films F-0, F-200, F-300 and F-350 despite the similarities in XRD, XPS and morphology. The ratio of NBE/DLE intensity is greatest for the F-200 sample. This can be associated with improved crystallinity and a lower concentration of radiative centres. F-350 exhibits the highest PL intensity and the lowest ratio of NBE/DLE and this can be due to a large number of point defects acting as radiative recombination centres. However, this is contrary to the high transmission and optical band gap of F-350, which do not suggest an increase in point defects. Instead, there may be lattice rearrangement from disordered oxygen vacancies to ordered defect structures such as shear planes. Formation of shear planes can annihilate the disordered oxygen vacancies associated with lower transmittance whilst providing sites for radiative recombination. F-400 shows a reduced intensity compared to F-350, which coincides with the appearance of nucleation in AFM. The lattice rearrangement involved in nucleation acts to eliminate vacancies from the structure and so can reduce the radiative

recombination centres. In addition, the new interfaces introduced will increase non-radiative recombination, and the Mo_4O_{11} phase itself is metallic.

In comparison of phase composition between the powders and films, the difference in the extent of reduction can be accounted for by the faster kinetics allowed by the large surface area of the film. This enables reduction to Mo metal in the film at 500 °C, whereas this is not seen in the powder sample. Conversely, MoO_2 content of the reduced films is low compared to the powders. This could be due to the analysis techniques, and there may be a larger amount of MoO_2 in the films than is detected. The low resolution of the grazing-incidence-XRD may not reveal small amounts of MoO_2 in the films, and atmospheric oxidation of MoO_2 can limit the detection by XPS, due to the surface sensitivity of the technique.

The mechanisms of reduction may also vary from powder to film. It is interesting that the first phase observed forming upon reduction of powders is MoO_2, yet we cannot conclude if this is also the case for MoO_3 films. Mo_4O_{11} is the first phase to be detected by XRD at the same point as MoO_2 is suggested by XPS. There is a possibility that MoO_2 is formed in the films prior to Mo_4O_{11} and that it is rapidly consumed in a further reaction. There is evidence for the formation of shear planes as seen by the structures in AFM at 400 °C, and it is likely that there is rearrangement of point defects at 350 °C, as shown by the high band gap and enhanced photoluminescence. Shear planes or extended defects in the films means that there would be a region of collapsed lattice necessarily in the structure bounded by the shear plane. This may take part in the nucleation of Mo_4O_{11}, in a mechanism similar to that proposed by Lalik *et al.* for MoO_3 powders, in which MoO_2 nucleates on the MoO_3 layers, and electron transfer from MoO_2 to MoO_3 allows the release of oxygen into the gas phase. Via transport of gaseous oxygen along the layers, the MoO_2 nuclei are re-oxidized to Mo_4O_{11} [21]. In the films here, the gas phase transport of oxygen would be easily accommodated by the layered microstructure. Movement along the layers would mean that before escaping, oxygen would

first encounter the collapsed structure at the shear plane in which Mo ions are available for oxidation and be recaptured.

4 Conclusions

MoO_3 powders and films have been synthesized from a simple aqueous solution route and the evolution of phase growth during reduction in hydrogen has been observed. There was increased roughness and loss of oxygen from the films before any new phases were detected by XRD. This contributes to an enhanced photoluminescence and decrease in the optical band gap. At higher temperatures the onset of MoO_2 formation is concurrent with Mo_4O_{11} nucleation. Extended planar defects within the films act as nucleation sites for Mo_4O_{11}. In any application utilizing MoO_{3-x} films, the morphological effect of reduction should be considered, as changes may result in degradation of properties or unstable devices. It has been shown here that increasing reduction of MoO_3 films causes restructuring of the films in order to accommodate oxygen vacancies. The resulting structures and phases mean that the optical band gap may not be as reduced as otherwise expected, and correspondingly optical properties such as photoluminescence may not give a linear response to increased reduction.

5 Acknowledgments

This work was performed within The Norwegian Research Centre for Solar Cell Technology project number 193829, a Centre for Environmentally-friendly Energy Research co-sponsored by the Norwegian Research Council and research and industry partners in Norway. NTNU NanoLab is acknowledged for support and subsidized use of their facilities. Augustinas Galeckas is thanked for performing the photoluminescence measurements.

References

[1] X. Haitao, Z. Xiang, Investigation of hole injection enhancement by MoO_3 buffer layer

in organic light emitting diodes, J. Appl. Phys. 114 (2013) 244505. doi:10.1063/1.4852835.

[2] L. Chibane, M.S. Belkaid, M. Pasquinelli, H. Derbal-Habak, J.-J. Simon, D. Hocine, O. Boudia, Development of Molybdenum trioxide (MoO_3) by spin coating method for photovoltaic application, Int. Conf. Renew. Energies Power Qual. (2012).

[3] F. Liu, S. Shao, X. Guo, Y. Zhao, Z. Xie, Efficient polymer photovoltaic cells using solution-processed MoO_3 as anode buffer layer, Sol. Energy Mater. Sol. Cells. 94 (2010) 842–845. doi:10.1016/j.solmat.2010.01.004.

[4] D. Xiang, C. Han, J. Zhang, W. Chen, Gap States Assisted MoO_3 Nanobelt Photodetector with Wide Spectrum Response, Sci. Rep. 4 (2014) 4891. doi:10.1038/srep04891.

[5] B. Dasgupta, Y. Ren, L.M. Wong, L. Kong, E.S. Tok, W.K. Chim, S.Y.Chiam, Detrimental Effects of Oxygen Vacancies in Electrochromic Molybdenum Oxide, J. Phys. Chem. C. 119 (2015) 10592–10601. doi:10.1021/acs.jpcc.5b02609.

[6] K. Ajito, L.A. Nagahara, D.A. Tryk, K. Hashimoto, A. Fujishima, Study of the Photochromic Properties of Amorphous MoO_3 Films Using Raman Microscopy, J. Phys. Chem. 99 (1995) 16383–16388. doi:10.1021/j100044a028.

[7] D.D. Yao, J.Z. Ou, K. Latham, S. Zhuiykov, A.P. O'Mullane, K. Kalantar-zadeh, Electrodeposited α- and ß-Phase MoO_3 Films and Investigation of Their Gasochromic Properties, Cryst. Growth Des. 12 (2012) 1865–1870. doi:10.1021/cg201500b.

[8] T. Ressler, J. Wienold, R.E. Jentoft, T. Neisius, Bulk Structural Investigation of the Reduction of MoO_3 with Propene and the Oxidation of MoO_2 with Oxygen, J. Catal. 210 (2002) 67–83. doi:10.1006/jcat.2002.3659.

[9] T. Brezesinski, J. Wang, S.H. Tolbert, B. Dunn, Ordered mesoporous α-MoO_3 with iso-oriented nanocrystalline walls for thin-film pseudocapacitors, Nat. Mater. 9 (2010) 146–151. doi:10.1038/nmat2612.

[10] L.E. Firment, A. Ferretti, Stoichiometric and Oxygen Deficient MoO_3(010) Surfaces, Surf. Sci. 129 (1983) 155–176.

[11] F. Werfel, E. Minni, Photoemission study of the electronic structure of Mo and Mo oxides, J. Phys. C Solid State Phys. 16 (1983) 6091–6100.

[12] T. Ressler, J. Wienold, R.E. Jentoft, F. Girgsdies, Evolution of Defects in the Bulk Structure of MoO_3 During the Catalytic Oxidation of Propene, Eur. J. Inorg. Chem. (2003) 301–312. doi:10.1002/ejic.200390040.

[13] S.Y. Chiam, B. Dasgupta, D. Soler, M.Y. Leung, H. Liu, Z.E. Ooi, L.M. Wong, C.Y. Jiang, K.L. Chang, J. Zhang, Investigating the stability of defects in MoO_3 and its role in organic solar cells, Sol. Energy Mater. Sol. Cells. 99 (2012) 197–203. doi:10.1016/j.solmat.2011.11.041.

[14] M. Kröger, S. Hamwi, J. Meyer, T. Riedl, W. Kowalsky, A. Kahn, Role of the deep-lying electronic states of MoO_3 in the enhancement of hole-injection in organic thin films, Appl. Phys. Lett. 95 (2009) 123301. doi:10.1063/1.3231928.

[15] P.-S. Wang, Y.-Y. Lo, W.-H. Tseng, M.-H. Chen, C.-I. Wu, Enhancing the incorporation compatibility of molybdenum oxides in organic light emitting diodes with gap state formations, J. Appl. Phys. 114 (2013) 063710. doi:10.1063/1.4817423.

[16] X.-B. Shi, M.-F. Xu, D.-Y. Zhou, Z.-K. Wang, L.-S. Liao, Improved cation valence state in molybdenum oxides by ultraviolet-ozone treatments and its applications in organic light-emitting diodes, Appl. Phys. Lett. 102 (2013) 233304.

doi:10.1063/1.4811267.

[17] J. Liu, X. Wu, S. Chen, X. Shi, J. Wang, S. Huang, X. Guo, G. He, Low-temperature MoO_3 film from a facile synthetic route for an efficient anode interfacial layer in organic optoelectronic devices, J. Mater. Chem. C. 2 (2014) 158–163. doi:10.1039/c3tc31580k.

[18] L.A. Bursill, Crystallographic shear in molybdenum trioxide, Proc. R. Soc. Lond. A. Math. Phys. Sci. 311 (1969) 267–290.

[19] T.H. Fleisch, G.J. Mains, An XPS study of the UV reduction and photochromism of MoO_3 and WO_3, J. Chem. Phys. 76 (1982) 780–786. doi:10.1063/1.443047.

[20] P.L. Gai, P.A. Labun, Electron Microscopy Studies Relating To Methanol Oxidation Over Ferric Molybdate and Molybdenum Trioxide Catalysts, J. Catal. 94 (1985) 79–96. doi:10.1016/0021-9517(85)90084-3.

[21] E. Lalik, Kinetic analysis of reduction of MoO_3 to MoO_2, Catal. Today. 169 (2011) 85–92. doi:10.1016/j.cattod.2010.09.013.

[22] W.V. Schulmeyer, H.M. Ortner, Mechanisms of the hydrogen reduction of molybdenum oxides, Int. J. Refract. Met. Hard Mater. 20 (2002) 261–269. doi:10.1016/S0263-4368(02)00029-X.

[23] M.J. Kennedy, S.C. Bevan, A Kinetic Study of the Reduction of Molybdenum Trioxide By Hydrogen, J. Less-Comon Met. 36 (1974) 23–30.

[24] L.C. Dufour, O. Bertrand, N. Floquet, Chemical Reactivity of (010)MoO_3: A Structural Study of the MoO_2 Formation in Molecular Hydrogen, Surf. Sci. 147 (1984) 396–412. doi:10.1017/CBO9781107415324.004.

[25] J. Słoczynski, W. Bobinski, Autocatalytic Effect in the Processes of Metal Oxide Reduction. II. Kinetics of Molybdenum Oxide Reduction, J. Solid State Chem. 92 (1991) 436–448. doi:10.1016/0022-4596(91)90350-Q.

[26] T. Ressler, R.E. Jentoft, J. Wienold, M.M. Günter, O. Timpe, In Situ XAS and XRD Studies on the Formation of Mo Suboxides during Reduction of MoO_3, J. Phys. Chem. B. 104 (2000) 6360–6370. doi:10.1021/jp000690t.

[27] J. Słoczynski, Kinetics and Mechanism of MoO_3 Reduction. Comments on "In Situ XAS and XRD Studies on the Formation of Mo Suboxides during Reduction of MoO_3", J. Phys. Chem. B. 106 (2002) 7718.

[28] E. Lalik, W.I.F. David, P. Barnes, J.F.C. Turner, Mechanisms of Reduction of MoO_3 to MoO_2 Reconciled?, J. Phys. Chem. B. 105 (2001) 9153–9156. doi:10.1021/jp011622p.

[29] J.J. Jasieniak, J. Seifter, J. Jo, T. Mates, A.J. Heeger, A Solution-Processed MoO_x Anode Interlayer for Use within Organic Photovoltaic Devices, Adv. Funct. Mater. 22 (2012) 2594–2605. doi:10.1002/adfm.201102622.

[30] H. Simchi, B.E. McCandless, T. Meng, J.H. Boyle, W.N. Shafarman, Characterization of reactively sputtered molybdenum oxide films for solar cell application, J. Appl. Phys. 114 (2013) 013503. doi:10.1063/1.4812587.

[31] Q. Fu, J. Chen, C. Shi, D. Ma, Room-Temperature Sol-Gel Derived Molybdenum Oxide Thin Films for Efficient and Stable Solution-Processed Organic Light-Emitting Diodes, ACS Appl. Mater. Interfaces. 5 (2013) 6024–6029. doi:10.1021/am4007319.

[32] J. Liang, F.-S. Zu, L. Ding, M.-F. Xu, X.-B. Shi, Z.-K. Wang, L.-S. Liao, Aqueous solution-processed MoO_3 thick films as hole injection and short-circuit barrier layer in

large-area organic light-emitting devices, Appl. Phys. Express. 7 (2014) 111601. doi:10.7567/APEX.7.111601.

[33] T. Grande, J.R. Tolchard, S.M. Selbach, Anisotropic Thermal and Chemical Expansion in Sr-Substituted $LaMnO_{3+\delta}$: Implications for Chemical Strain Relaxation, Chem. Mater. 24 (2012) 338–345. doi:10.1021/cm2030608.

[34] R. Coquet, D.J. Willock, The (010) surface of α-MoO_3, a DFT + U study, Phys. Chem. Chem. Phys. 7 (2005) 3819–3828. doi:10.1039/b511044k.

[35] L.A. Bursill, Electron Microscope Study of an Homologous Series of Shear Structures based on Molybdenum Trioxide, Acta Crystallogr. A28 (1972) 187–191. doi:10.1107/S0567739472000403.

[36] P.L. Gai-Boyes, Defects in Oxide Catalysts: Fundamental Studies of Catalysis in Action, Catal. Rev. 34 (1992) 1–54. doi:10.1080/01614949208021918.

[37] D. Wang, D.S. Su, R. Schlögl, Crystallographic Shear Defect in Molybdenum Oxides: Structure and TEM of Molybdenum Sub-oxides $Mo_{18}O_{52}$ and Mo_8O_{23}, Cryst. Res. Technol. 38 (2003) 153–159. doi:10.1002/crat.200310018.

[38] P.F. Carcia, E.M. McCarron, Synthesis and Properties of Thin Film Polymorphs of Molybdenum Trioxide, Thin Solid Films. 155 (1987) 53–63. doi:10.1016/0040-6090(87)90452-4.

[39] S. Tiwari, R. Master, R.J. Choudhary, D.M. Phase, B.L. Ahuja, Effect of oxygen partial pressure and Fe doping on growth and properties of metallic and insulating molybdenum oxide thin films, J. Appl. Phys. 111 (2012) 083905. doi:10.1063/1.3703669.

[40] S.-Y. Lin, Y.-C. Chen, C.-M. Wang, P.-T. Hsieh, S.-C. Shih, Post-annealing effect upon optical properties of electron beam evaporated molybdenum oxide thin films, Appl. Surf. Sci. 255 (2009) 3868–3874. doi:10.1016/j.apsusc.2008.10.069.

[41] M. Rouhani, Y.L. Foo, J. Hobley, J. Pan, G.S. Subramanian, X. Yu, A. Rusydi, S. Gorelik, Photochromism of amorphous molybdenum oxide films with different initial Mo^{5+} relative concentrations, Appl. Surf. Sci. 273 (2013) 150–158. doi:10.1016/j.apsusc.2013.01.218.

[42] G.E. Buono-Core, G. Cabello, A.H. Klahn, A. Lucero, M. V Nuñez, B. Torrejón, C. Castillo, Growth and characterization of molybdenum oxide thin films prepared by photochemical metal-organic deposition (PMOD), Polyhedron. 29 (2010) 1551–1554. doi:10.1016/j.poly.2010.01.036.

[43] H. Ohtsuka, Y. Sakurai, Characterization of MoO_{3-x} Thin Films, Jpn. J. Appl. Phys. 40 (2001) 4680–4683.

[44] I. Kostis, N. Vourdas, G. Papadimitropoulos, A. Douvas, M. Vasilopoulou, N. Boukos, D. Davazoglou, Effect of the Oxygen Sub-Stoichiometry and of Hydrogen Insertion on the Formation of Intermediate Bands within the Gap of Disordered Molybdenum Oxide Films, J. Phys. Chem. C. 117 (2013) 18013–18020. doi:10.1021/jp407354j.

[45] A. Luque, A. Martí, The Intermediate Band Solar Cell: Progress Toward the Realization of an Attractive Concept, Adv. Mater. 22 (2010) 160–174. doi:10.1002/adma.200902388.

[46] Z.M. Hanafi, M.A. Khilla, M.H. Askar, The Thermal Decomposition of Ammonium Heptamolybdate, Thermochim. Acta. 45 (1981) 221–232. doi:10.1016/0040-6031(81)85083-6.

[47] J. Meyer, S. Hamwi, M. Kröger, W. Kowalsky, T. Riedl, A. Kahn, Transition Metal Oxides for Organic Electronics: Energetics, Device Physics and Applications, Adv. Mater. 24 (2012) 5408–5427. doi:10.1002/adma.201201630.

[48] D.O. Scanlon, G.W. Watson, D.J. Payne, G.R. Atkinson, R.G. Egdell, D.S.L. Law, Theoretical and Experimental Study of the Electronic Structures of MoO_3 and MoO_2, J. Phys. Chem. C. 114 (2010) 4636–4645. doi:10.1021/jp9093172.

[49] J. Dang, G.-H. Zhang, K.-C. Chou, R.G. Reddy, Y. He, Y. Sun, Kinetics and mechanism of hydrogen reduction of MoO_3 to MoO_2. *Int. J. Refract. Met. Hard Mater.* 41, (2013) 216–223. doi:10.1016/j.ijrmhm.2013.04.002

[50] M. Itoh, K. Hayakawa, S. Oishi, Optical properties and electronic structures of layered MoO_3 single crystals, J. Phys. Condens. Matter. 13 (2001) 6853–6864. doi:10.1088/0953-8984/13/31/319.

[51] I. Navas, R. Vinodkumar, V.P. Mahadevan Pillai, Self-assembly and photoluminescence of molybdenum oxide nanoparticles, Appl. Phys. A Mater. Sci. Process. 103 (2011) 373–380. doi:10.1007/s00339-011-6345-9.

[52] M. Labanowska, Paramagnetic defects in MoO_3-revisited, Phys. Chem. Chem. Phys. 1 (1999) 5385–5392.

[53] M. Dieterle, G. Weinberg, G. Mestl, Raman spectroscopy of molybdenum oxides Part I. Structural characterization of oxygen defects in MoO_{3-x} by DR UV/VIS, Raman spectroscopy and X-ray diffraction, Phys. Chem. Chem. Phys. 4 (2002) 812–821. doi:10.1039/b107012f.

[54] R.K. Sharma, G.B. Reddy, Effect of substrate temperature on the characteristics of α-MoO_3 hierarchical 3D microspheres prepared by facile PVD process, J. Alloys Compd.

598 (2014) 177–183. doi:10.1016/j.jallcom.2014.01.238.

[55] S. Bai, S. Chen, L. Chen, K. Zhang, R. Luo, D. Li, C.C. Liu, Ultrasonic synthesis of MoO_3 nanorods and their gas sensing properties, Sensors Actuators, B Chem. 174 (2012) 51–58. doi:10.1016/j.snb.2012.08.015.

[56] T. Anh Tran, K. Krishnamoorthy, Y.W. Song, S.K. Cho, S.J. Kim, Toxicity of Nano Molybdenum Trioxide toward Invasive Breast Cancer Cells, ACS Appl. Mater. Interfaces. 6 (2014) 2980–2986. doi:10.1021/am405586d.

[57] M.M.Y.A. Alsaif, K. Latham, M.R. Field, D.D. Yao, N.V. Medehkar, G.A. Beane, R.B. Kaner, S.P. Russo, J.Z. Ou, K. Kalantar-zadeh, Tunable Plasmon Resonances in Two-Dimensional Molybdenum Oxide Nanoflakes, Adv. Mater. 26 (2014) 3931–3937. doi:10.1002/adma.201306097.

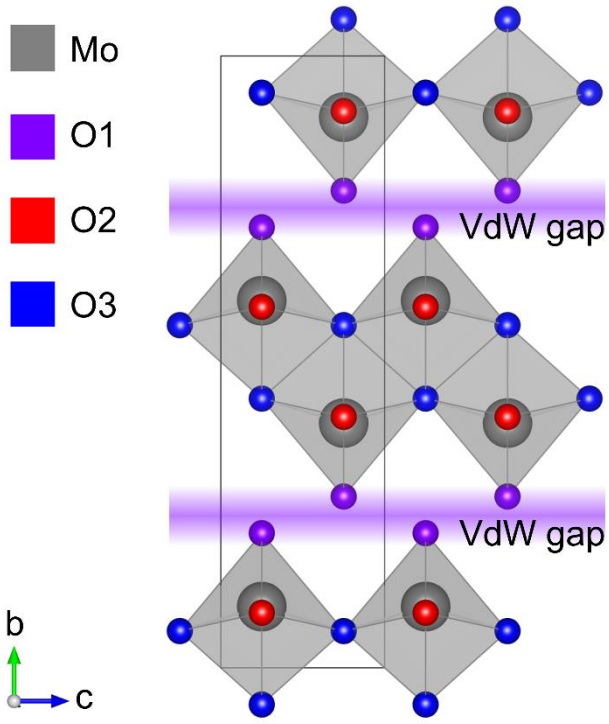

Figure 1. Crystal structure of MoO_3 showing the three inequivalent oxygen positions (O1, O2 and O3) and the van der Waals (VdW) gap.

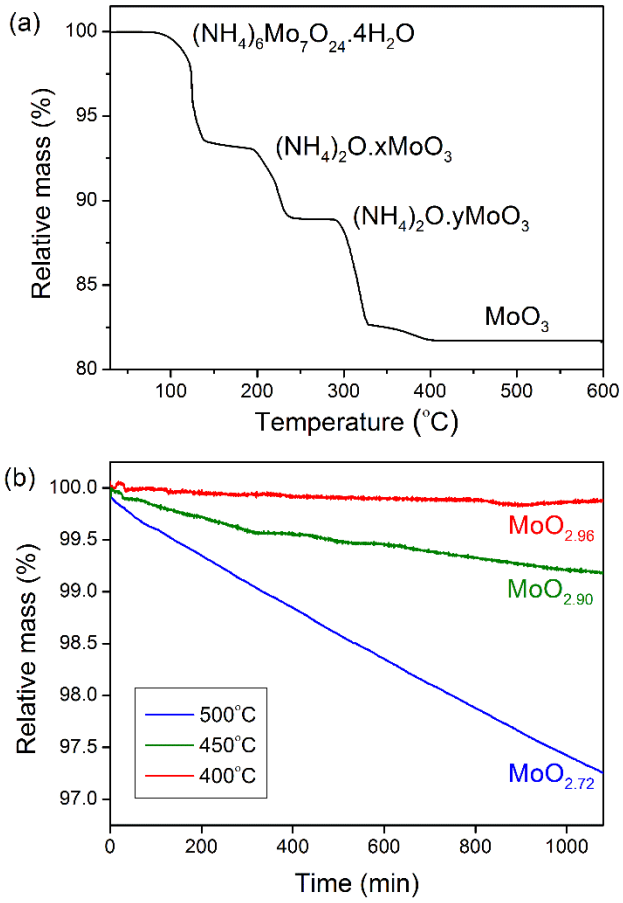

Figure 2. Thermogravimetric analysis a) Mass loss during decomposition of ammonium heptamolybdate in heating to 600 °C in synthetic air. b) Mass loss of MoO_3 during reduction in 2 % H_2/98 % Ar atmosphere, holding at 400 °C, 450 °C and 500 °C for 18 h, with estimates of the end stoichiometry displayed.

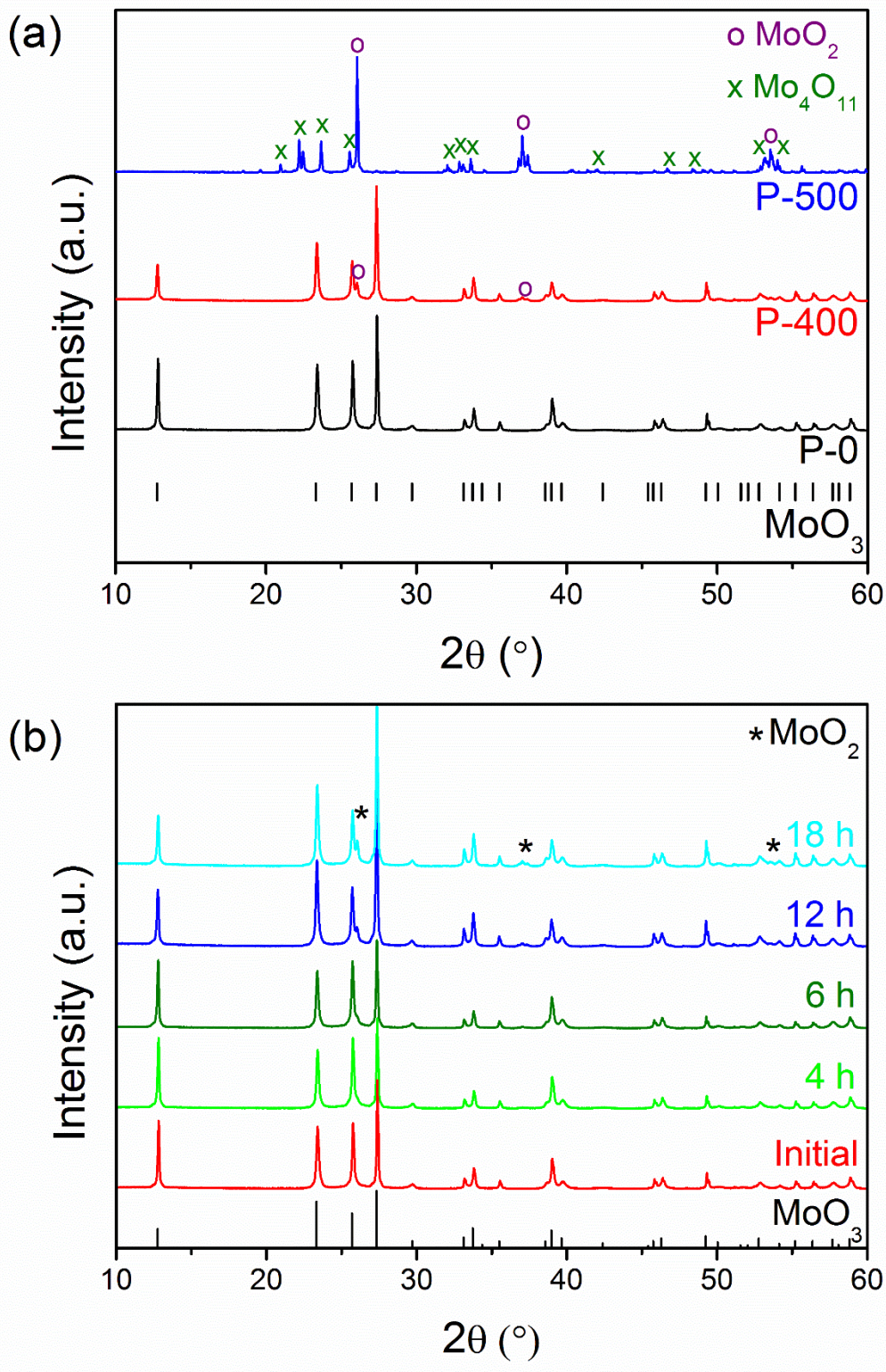

Figure 3. X-ray diffractograms a) MoO_3 powders without annealing (P-0) and annealed in 5 % H_2/Ar for 18 h at 400 °C (P-400) and 500 °C (P-500). b) MoO_3 powders before and after annealing in 5 % H_2/95 % Ar at 400 °C, for various annealing times.

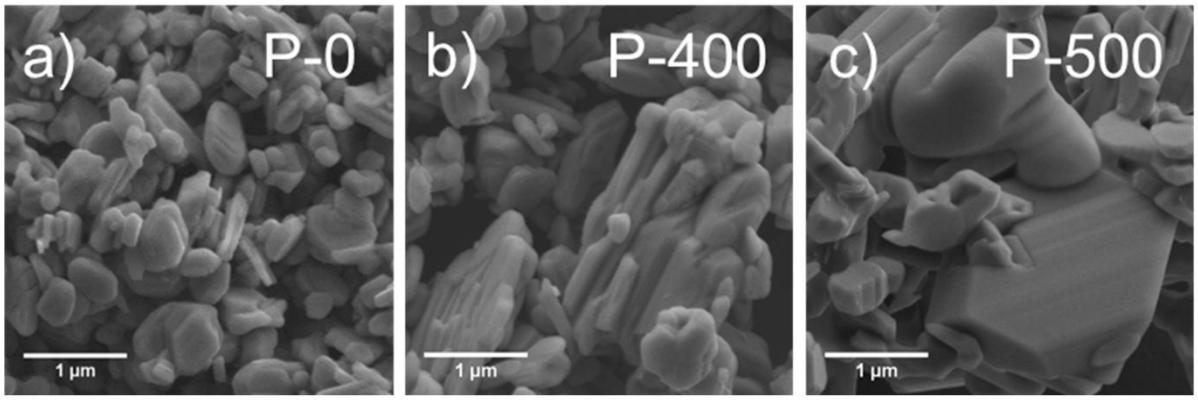

Figure 4. Scanning electron micrographs of MoO_3 powder, a) P-0, and reduced powders, b) P-400, and c) P-500.

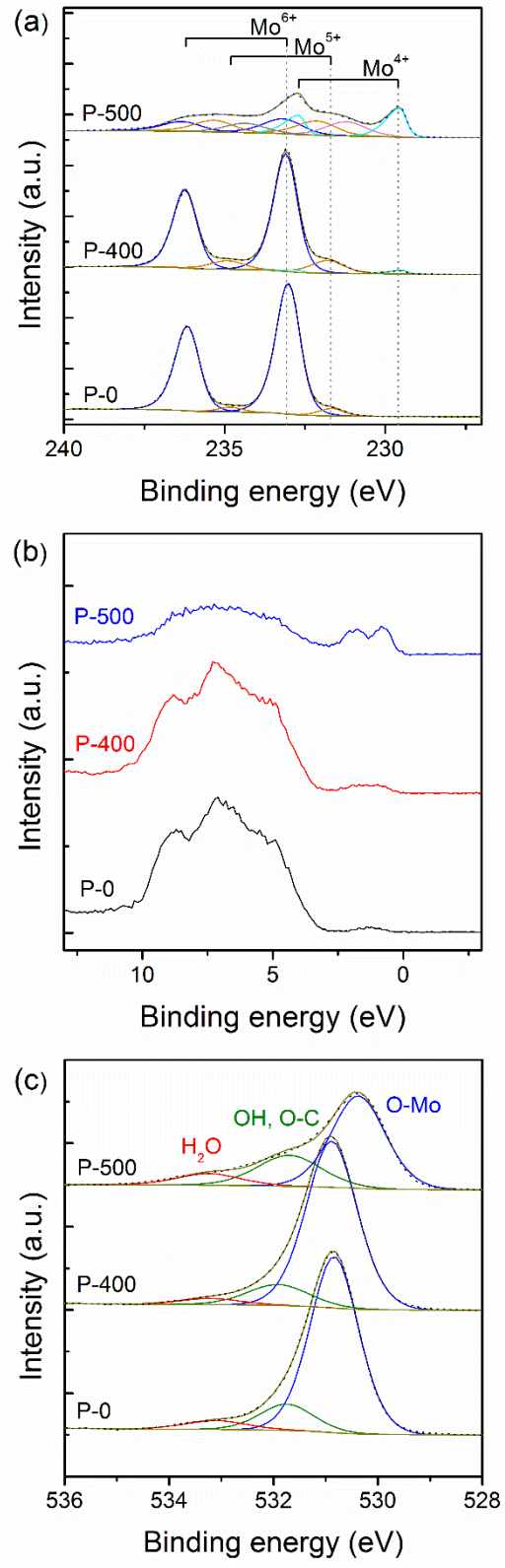

Figure 5. XPS spectra of the powders P-0, P-400 and P-500. a) Mo 3*d* peaks with peak fitting. b) The valence band region. c) O 1*s* peaks. The binding energy of the O-Mo component for P-0, P-400, and P-500 is at 530.84, 530.89, and 530.37 eV, respectively.

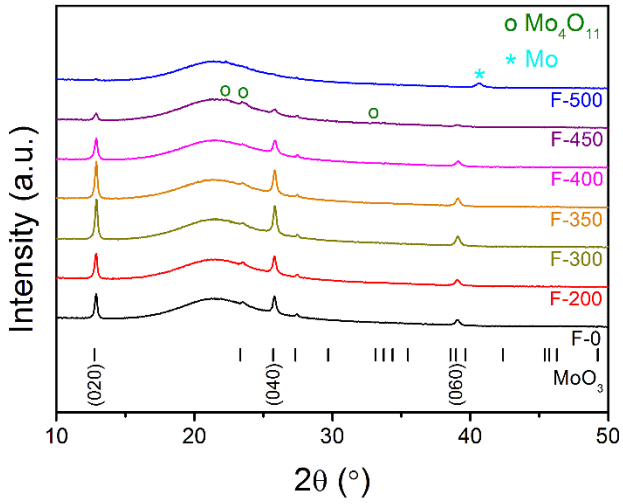

Figure 6. X-ray diffractograms of an unreduced MoO_3 film, F-0, and reduced films, F-200 to F-500.

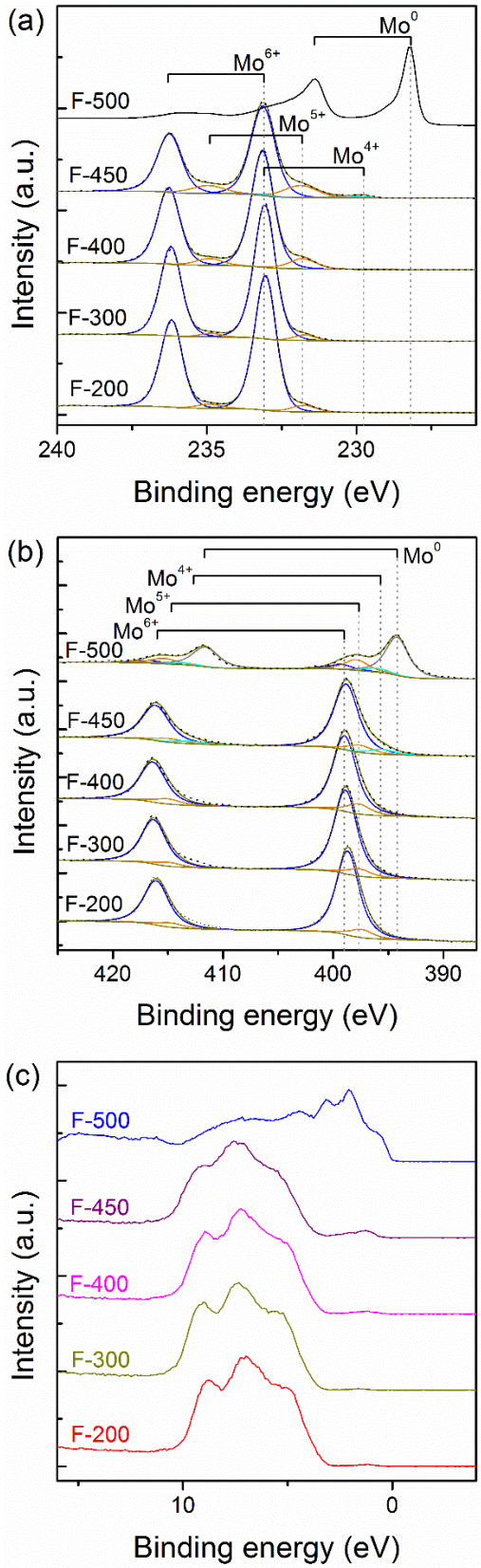

Figure 7. XPS spectra of MoO_3 films after hydrogen reduction treatment. a) Mo 3*d* peaks. b) Mo 3*p* peaks. c) Valence band region.

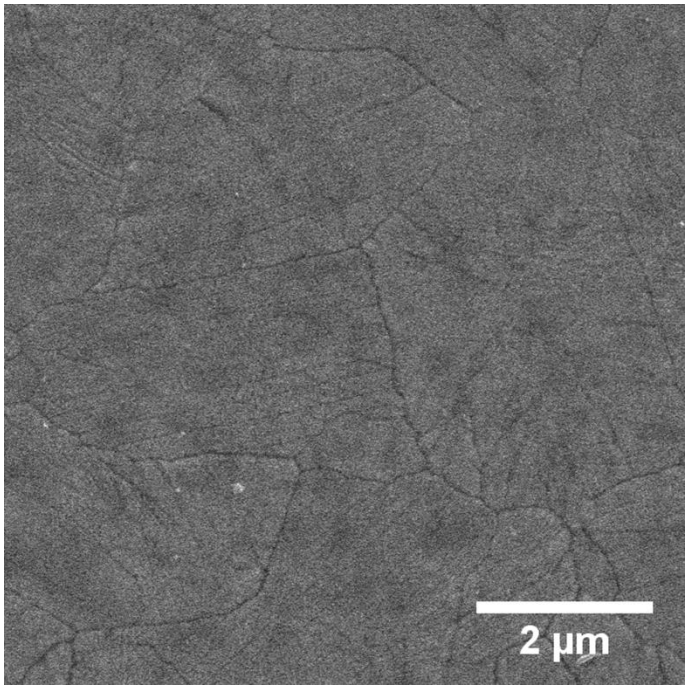

Figure 8. Scanning electron micrograph showing homogeneity and grain structure of a MoO_3 film.

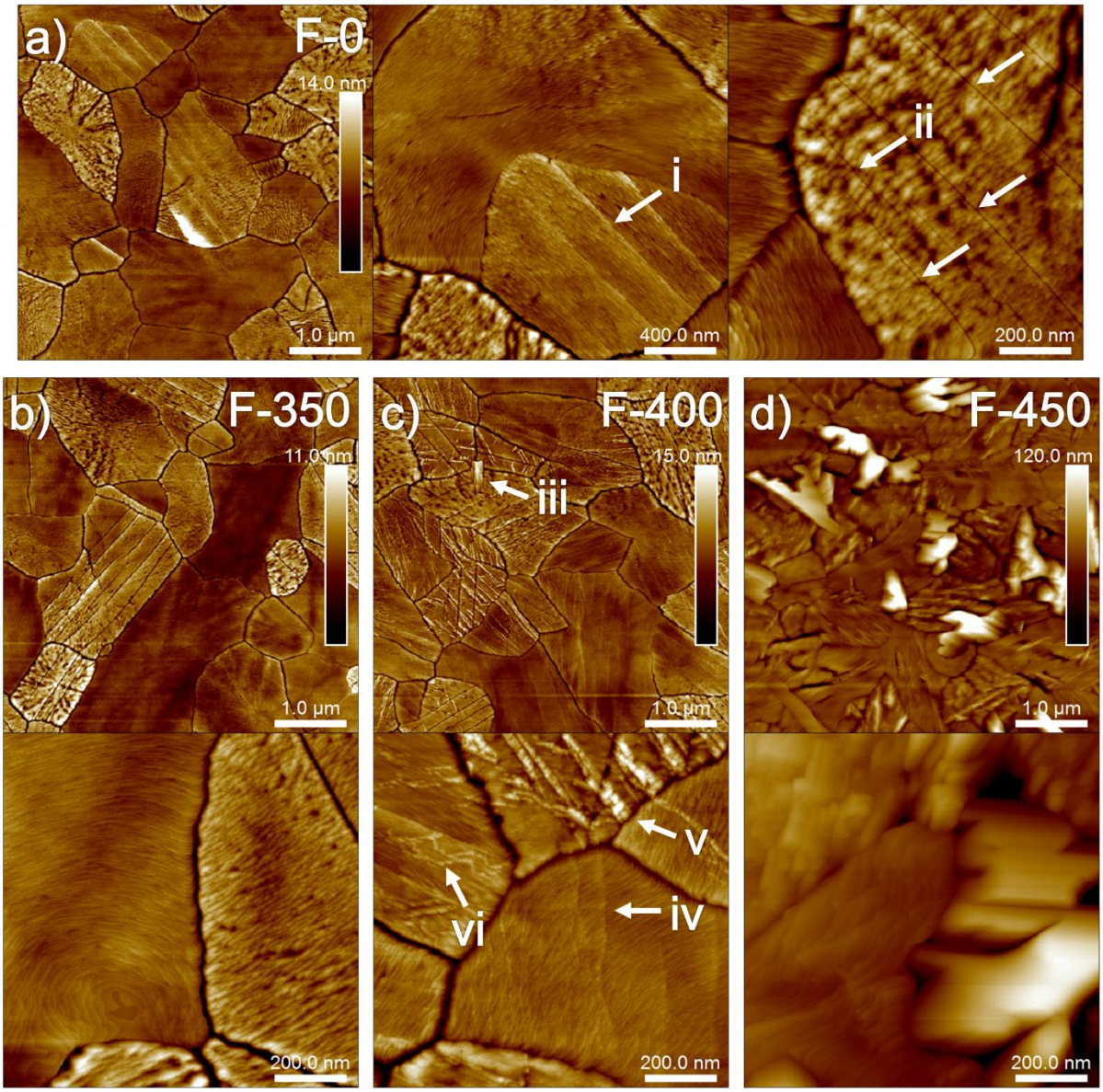

Figure 9. AFM images of molybdenum oxide films. a) MoO_3 film sample F-0, (i) arrow indicating nanocrystallite steps. (ii) arrows indicating misfit defects. Samples after reduction at various temperatures, b) F-350; c) F-400, with arrows at (iii) indicating a nucleation site, (iv) shear structures and (v-vi) phase nucleation along shear steps; d) F-450.

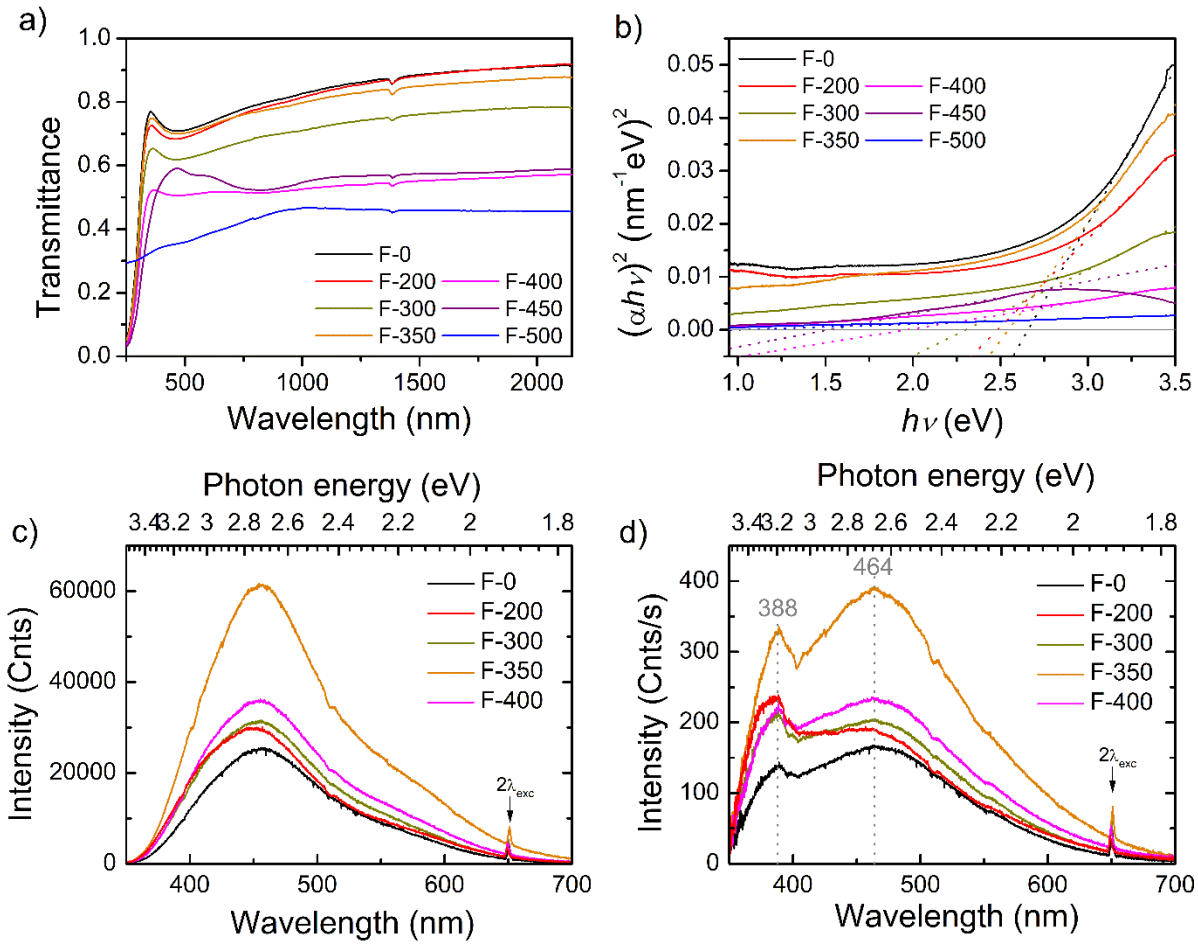

Figure 10. Optical measurements of the reduced films. a) Transmittance spectra, b) Tauc plot, c) photoluminescence spectra, d) photoluminescence spectra corrected for instrument spectral response.

Table 1. Spectral fitting of Mo *3d* peaks: Mo $3d_{5/2}$ binding energy (eV), FWHM value (eV), and the relative content of 4+, 5+ and 6+ oxidation states of Mo (%).

Sample name	**Mo^{4+}** BE (eV), FWHM (eV) Content (%)	**Mo^{5+}** BE (eV), FWHM (eV) Content (%)	**Mo^{6+}** BE (eV), FWHM (eV) Content (%)
P-0	---	231.67 0.87 5.3 %	232.99 0.87 94.7 %
P-400	229.47 0.47 2.1 %	231.75 1.19 12.9 %	233.07 0.86 85.0 %
P-500	229.52 0.52 48.7 %	232.09 1.4 26.4 %	233.14 1.4 24.9 %

Table 2. Spectral fitting of XPS Mo 3*d* and Mo 3*p* peaks of MoO_3 films: Mo $3d_{5/2}$ and Mo $3p_{3/2}$ binding energy (eV), FWHM value (eV), and the relative content of 0, 4+, 5+ and 6+ oxidation states of Mo (%).

	Mo $3d_{5/2}$				**Mo $3p_{3/2}$**		
Sample name	Mo^{4+} BE (eV), FWHM (eV) Content (%)	Mo^{5+} BE (eV), FWHM (eV) Content (%)	Mo^{6+} BE (eV), FWHM (eV) Content (%)	Mo^{0} BE (eV), FWHM (eV) Content (%)	Mo^{4+} BE (eV), FWHM (eV) Content (%)	Mo^{5+} BE (eV), FWHM (eV) Content (%)	Mo^{6+} BE (eV), FWHM (eV) Content (%)
F-200	---	231.75 0.96 5.3 %	233.03 0.83 94.7 %	---	---	397.44 2.44 9.8 %	398.69 2.44 90.2 %
F-300	---	231.72 0.81 3.9 %	233.05 0.83 96.1 %	---	---	397.64 2.47 8.1 %	398.89 2.47 91.9 %
F-400	---	231.79 1.04 9.4 %	233.13 0.87 90.6 %	---	---	397.71 2.51 11.7 %	398.96 2.51 88.3 %
F-450	229.76 0.59 3.6 %	231.84 1.29 15.1%	233.12 0.94 81.3 %	---	395.58 2.62 6.2 %	397.58 2.62 9.2 %	398.83 2.62 84.6 %
F-500	--- --- ---	--- --- ---	--- --- ---	394.21 2.46 64.9 %	396.06 2.46 6.8 %	397.91 2.46 19.8 %	399.31 2.46 8.5 %

Table 3. Film samples with reduction temperature and root mean square roughness values, measured by AFM over a 10 μm x 10 μm area

Sample name	Reduction temperature (°C)	Thickness (nm ± 5 nm)	RMS roughness, Rq, (nm)	Optical band gap, E_g, (eV ± 0.1 eV)
F-0	-	60	1.53	2.7
F-200	200	58	1.58	2.5
F-300	300	56	1.61	2.3
F-350	350	55	1.84	2.5
F-400	400	61	1.91	2.0
F-450	450	-	19.2	1.5
F-500	500	-	-	1.0